Energy 301 (2024) 131734

Contents lists available at ScienceDirect

Energy

journal homepage: www.elsevier.com/locate/energy

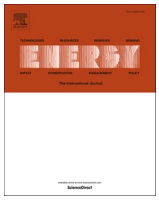

Coupled optimization of auxiliary channels and porosity gradient of GDL for PEMFC

Cong Tian [a], Fang Yuan [a,*], Tianlun Deng [a], Qianhui He [a], Cen Hu [a], Yong Chen [b], Wei Liu [a]

[a] School of Energy and Power Engineering, Huazhong University of Science and Technology, Wuhan, 430074, China
[b] Wuhan Second Ship Design and Research Institute, Wuhan, 430074, China

ARTICLE INFO

Handling Editor: Dr. A. Olabi

Keywords:
Proton exchange membrane fuel cell
Coupling optimization
Artificial neural network
Auxiliary channels
Porosity gradient

ABSTRACT

In this study, we proposed a novel under-rib auxiliary channel and developed a systematic methodology combining computational fluid dynamics (CFD), an artificial neural network (ANN), and a particle swarm optimization (PSO) algorithm for the coupled optimization of the auxiliary-channel structure and gas diffusion layer (GDL) porosity gradient in a proton exchange membrane fuel cell (PEMFC). First, we developed a three-dimensional multiphase numerical model of a non-isothermal parallel flow-field PEMFC. ANN was then applied to obtain a mapping relationship between auxiliary channels structure, GDL porosity gradient and output performance of PEMFC with finite CFD data. Finally, PSO was employed to perform an optimization search to determine the optimal parameter pairing, resulting in a 16.7 % increase in maximum power density and a 20.6 % increase in the current operating range. In addition, the optimized PEMFC exhibited superior mass transfer and water removal capabilities, where the average oxygen concentration in the intermediate section of cathode GDL was increased by 33.3 % and the maximum liquid water saturation was reduced by 23.5 %. Moreover, the coupled optimization of the auxiliary channels and the GDL porosity gradient can increase power density by at least 8.7 % and current density by 9.1 % compared to single component optimization.

1. Introduction

Due to the energy crisis and environmental pollution caused by excessive use of fossil fuels, the development of sustainable energy sources has attracted widespread interest [1]. Hydrogen stands out as one of the most promising secondary energy sources due to its high calorific value, environmental friendliness, and storability [2]. Proton exchange membrane fuel cells (PEMFCs) directly convert hydrogen energy into electricity. They offer advantages such as low operating temperatures, clean and pollution-free operation, high power density, and high efficiency, and are now widely used in transportation, housing, and power generation [3–5].

During actual operation, the cathode side of a PEMFC is prone to flooding and exhibits poor mass-transfer capability, potentially leading to inhomogeneous reactant distribution and diminished output performance [6–8]. The ability of a PEMFC to transfer water and reactants is significantly influenced by the flow channel design; hence, optimizing the geometry of the flow channel is important for improving output performance [9,10]. Chiu et al. [11] studied three conventional flow fields, namely, parallel, cross-finger, and serpentine, and analyzed the effects of channel width, height, and aspect ratio on cell performance and water removal. Zhou et al. [12] proposed a novel opposite sinusoidal wave flow channel to improve the mass transfer and water-removal capacity of PEMFCs. Their results indicated that increasing the amplitude and decreasing the period could effectively improve the mass-transfer capacity and performance of the PEMFC. Wan et al. [13] proposed a new M-like channel based on minimum entropy generation, demonstrating stronger heat and mass-transfer performance and a 21.3 % higher maximum output power compared to conventional flow channels. Zuo et al. [14] investigated the effect of auxiliary flow-field blocks on cell pressure drop, reactant distribution, and liquid water removal, achieving a 21.7 % improvement in cell output performance. Liao et al. [15] proposed an auxiliary-channel design based on a wave-like flow field and investigated its effects on water removal using the volume-of-fluid method. Their results showed that the subchannel enhanced drainage performance by overcoming wall adhesion through an enhanced pressure differential.

As another key component of PEMFCs, the gas diffusion layer (GDL) serves important functions such as providing structural support, facilitating gas diffusion, and discharging reaction by-products, thereby significantly impacting the mass-transfer performance of PEMFCs

* Corresponding author.
E-mail address: yuanf@hust.edu.cn (F. Yuan).

https://doi.org/10.1016/j.energy.2024.131734
Received 17 January 2024; Received in revised form 12 April 2024; Accepted 20 May 2024
Available online 20 May 2024

Nomenclature

Symbols

u	velocity, m/s
S	Source term
M	molar mass, kg/mol
J	exchange current density, A/m^3
R	ideal gas constant, J/(mol•K)
F	Faraday constant, C/mol
T	temperature, K
p	pressure, Pa
c_p	constant pressure specific heat capacity, J/(kg•K)
I	current density, A/m^2
s	liquid water saturation
K	permeability, 1/m^2
c_r	condensation rate constant, 1/s
P_{mv}	partial pressure of water vapor, Pa
P_{sat}	saturation pressure, Pa
P_c	capillary pressure, Pa
A	water activity
Y	mass fraction
D	diffusion coefficient
Q	mass flow rate, kg/s
R_{ohm}	ohmic resistance, Ω
h_{rea}	heat production by electrochemical reaction, J
EW	equivalent molecular weight of electrolyte, kg/mol
h_L	latent heat of water phase transition, J
n^d	electro-osmotic drag coefficient
N	number of auxiliary channels under rib
W	auxiliary channel width, mm
H	auxiliary channel height, mm
k	GDL porosity gradient

Greek Letters

ε	porosity
ρ	density, kg/m^3
λ	thermal conductivity, W/(m•K)
α	water content
μ	dynamic viscosity, Pa•s
σ	proton conductivity, S/m
φ	electrical potential, V
ζ	stoichiometric ratio

Subscript and Superscripts

w	water
i	species (H_2, O_2, H_2O)
a	anode
c	cathode
sol	solid
mem	membrane
ref	reference
eff	effective

Abbreviations

CFD	computational fluid dynamics
ANN	artificial neural network
LHS	latin hypercube sampling
PSO	particle swarm optimization
BP	bipolar plate
FC	flow channel
GDL	gas diffusion layer
CL	catalyst layer
PEMFC	proton exchange membrane fuel cell

[16–18]. Besides optimizing the geometric parameters of the GDL [19–21], the gradient effect within the GDL also notably impacts cell performance. Li et al. [22] developed a theoretical optimization model for the porosity distribution of the cathode GDL using the variational principle, resulting in significant improvements in both output performance and the uniformity of oxygen and current density distributions. Ko et al. [23] performed an in situ visualization analysis of pore gradient GDLs to investigate the effect of porosity gradient on cell performance, finding that the medium pore gradient GDL performed best under different humidity conditions. Xiang et al. [24] revealed that the porosity distribution and contact angle significantly affect liquid water distribution and water saturation in the GDL, noting that liquid water accumulation tends to occur in high-porosity regions.

The above literature review demonstrates optimizing the flow channel and GDL structure alone can significantly improve the performance of PEMFC. However, the flow and mass fields of these two components will interact with each other, therefore some researchers have tried to optimize both flow channel and diffusion layer. For instance, Zhang et al. [25] investigated the coupling effect of wedge-shaped fins and GDL porosity in a single-channel PEMFC. Their findings showed that the effect of GDL porosity on improving PEMFC performance was greater than that of wedge-shaped fins, although the effect of GDL porosity weakened as porosity increased. Xu et al. [26] optimized the depth and location of grooves in a GDL based on an optimized wave-shaped flow channel structure, thereby enhancing cell performance.

3D simulation models can accurately analyze the coupled processes of heat transfer, mass transfer, flow, and electrochemical reactions within a PEMFC. These models are useful for optimizing flow channel structures, GDL structures, and porosity distributions. However, due to cost constraints, most previous studies have examined only a limited number of discrete design points and neglected the coupling relationships between different variables, potentially leading to local optimum solutions. To avoid this problem, many researchers have employed intelligent optimization algorithms to enhance the flow field and performance of PEMFCs [27–29]. For example, Cai et al. [30] investigated a bio-inspired wave-like channel based on the fins of cuttlefish using a genetic algorithm, revealing that such a structure resulted in lower flow resistance and higher output efficiency. Liu et al. [31] utilized a neural network agent model and a fast non-dominated sorting genetic algorithm (NSGA-II) to simultaneously optimize flow uniformity, diffusion flux, and ohmic resistance, showing improved power and a more uniform current density. The particle swarm optimization (PSO) algorithm has also been established as a viable method for optimizing the performance of PEMFC [32]. Wilberforce et al. [33] applied the PSO algorithm to determine the optimal operating conditions for PEMFCs, resulting in a 9.4 % improvement in cell performance.

Given these studies, it is evident that both the flow channel structure and GDL porosity distribution have significantly affect the output performance of PEMFC. However, to the author's knowledge, research on simultaneously optimizing both elements while examining their coupling effects is insufficient. Therefore, in this paper, a PEMFC model featuring under-rib auxiliary channels and GDL porosity gradient is established combined with computational fluid dynamics (CFD). In order to reduce computation time and avoid falling into local optimality, the conventional CFD model is replaced by the surrogate model established by artificial neural network (ANN) with a small amount of simulation data. Then, the particle swarm optimization (PSO) algorithm could be used to find the optimal combination of the operating and structure parameters. Finally, the original case, the single component

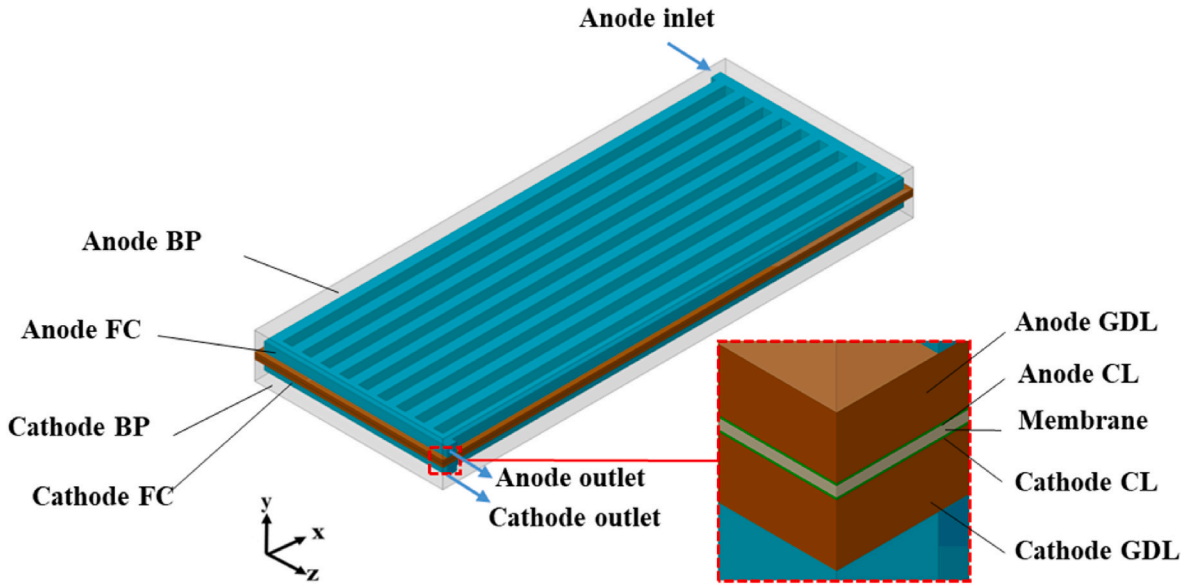

Fig. 1. Schematic diagram of PEMFC structure.

Table 1
Geometric parameters of PEMFC.

Parameters	Value/mm
Cell length	50
Cell width	20
Channel width	1
Channel height	1
Rib width	1
BP height	2
GDL thickness	0.19
CL thickness	0.01
Membrane thickness	0.05

optimization results and the coupled optimization result are analyzed and compared.

2. Model development

2.1. Geometric models and assumptions

Parallel-flow-field PEMFCs have the advantages of simple structures and low flow pressure drops. However, their inhomogeneous reactant distributions and weak water removal capability may result in poor output performance. Referring to dimensions of parallel-flow-field PEMFC in other literature [22,34,35], physical model of a typical parallel-flow-field PEMFC with ten channels is presented, as depicted in Fig. 1. The model includes key components such as bipolar plates (BPs), flow channels (FCs), GDLs, catalyst layers (CLs), and proton exchange membrane. The relevant geometric parameters are detailed in Table 1. Considering that the oxygen diffusion coefficient is much smaller than the hydrogen diffusion coefficient, which leads to the mass transfer resistance on the cathode side to be the main reason for insufficient mass transfer, it is more efficient to optimize the cathode side [36]. Therefore, the optimization in this study focuses on optimizing only the cathode FC and GDL while keeping the anode side unchanged.

Numerous literature [14,37] suggest that auxiliary channels can help improve mass transfer capability and homogeneity of reactants, therefore, this paper proposes the under-rib auxiliary channels adjacent to GDL for flow channel optimization. Besides, the porosity gradient along the GDL thickness direction can effectively improve the capillary diffusion and water removal of PEMFC [38]. Therefore, we compare a coupling-optimized parallel-flow-field (COPFF) PEMFC, featuring under-rib auxiliary channels and a GDL with gradient porosity, against a normal parallel-flow-field (NPFF) PEMFC. The designs for the cathode flow field and porosity gradient are schematically illustrated in Figs. 2 and 3, respectively, where N, H, W are the number of auxiliary channels under a rib, the height and the width of the auxiliary channels, respectively, and k is the GDL porosity gradient determined by porosity close to CL, ε_1, higher porosity near FC, ε_2, and the thickness of GDL, h_{GDL}.

To simplify the model, the following assumptions were made: The PEMFC operates under steady-state conditions. The flow within PEMFC is laminar and incompressible. The gas reactants are treated as ideal gases. The GDLs, CLs, and membranes are isotropic and homogeneous materials. The effects of gravity on species diffusion and reaction processes are neglected.

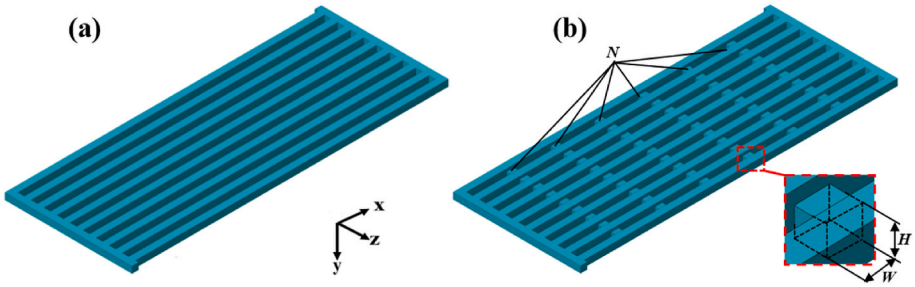

Fig. 2. Schematic diagrams of cathode flow-field structures (a) NPFF, (b) COPFF.

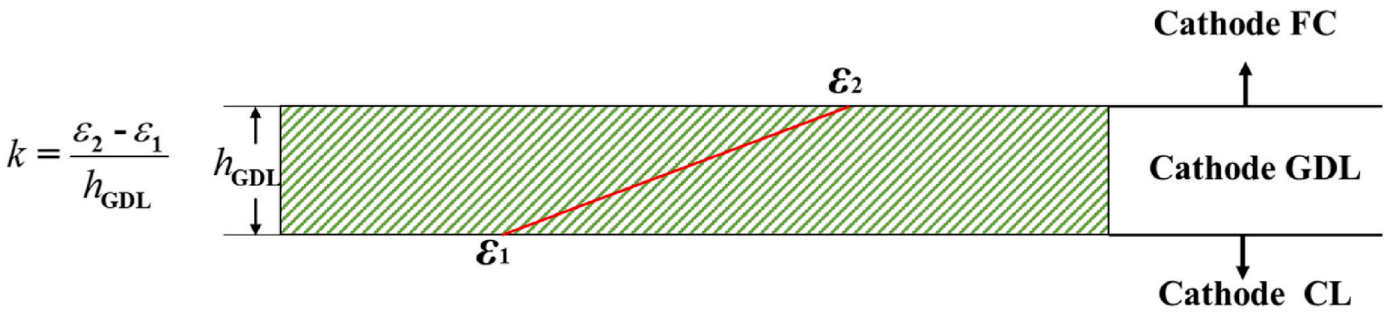

Fig. 3. Schematic diagram of cathode GDL with linear gradient porosity of k, where $k=(\varepsilon_2 - \varepsilon_1)/h_{GDL}$.

2.2. Governing equations

To simulate the intricate interplay of flow, heat transfer, mass transfer, and electrochemical reactions within the PEMFC, a 3D multi-phase mathematical model was established. The governing equations mainly include basic conservation equations and the liquid water transport equations.

Mass conservation equation :

$$\nabla \cdot (\varepsilon \rho \vec{u}) = S_m \tag{1}$$

where ε is porosity of porous media and for the flow channel, $\varepsilon = 1$. ρ and u are density and velocity, respectively, while S_m is the mass source term.

Momentum conservation equation :

$$\nabla \cdot (\varepsilon \rho \vec{u}\vec{u}) = -\varepsilon \nabla p + \nabla \cdot (\varepsilon \mu \nabla \vec{u}) + S_{mom} \tag{2}$$

where p represents pressure, μ indicates dynamic viscosity and S_{mom} is the momentum source term.

Energy conservation equation :

$$\nabla \cdot \left(\varepsilon \rho c_p \vec{u} T\right) = \nabla \cdot \left(\lambda^{eff} \cdot \nabla T\right) + S_T \tag{3}$$

where c_p, T, λ^{eff} are constant pressure specific heat capacity, temperature and effective thermal conductivity, respectively. S_T denotes the energy source term.

Species conservation equation :

$$\nabla \cdot (\varepsilon \rho \vec{u} Y_i) = \nabla \cdot \left(D_i^{eff} \nabla Y_i\right) + S_i \tag{4}$$

where Y_i and D_i are the mass fraction and diffusion coefficient of species i ($i = H_2$, O_2 and H_2O), while S_i is the concentration source term.

Charge conservation equation :

$$\nabla \cdot (\sigma_{sol} \nabla \varphi_{sol}) + S_{sol} = 0 \tag{5}$$

$$\nabla \cdot (\sigma_{mem} \nabla \varphi_{mem}) + S_{mem} = 0 \tag{6}$$

where σ and φ are conductivity and electrical potential, respectively, while the subscript sol and mem represent solid phase and membrane phase, respectively. S_{sol} is the electronic current source term while S_{mem} is the protonic current source term.

In FCs of PEMFC, liquid water transport is mainly driven by convection, which is controlled by the following equation:

$$\nabla \cdot (\rho \vec{u} s) = S_l \tag{7}$$

where S_l is water saturation source term, standing for the net evaporation of liquid water. In porous media region, convection term replaced by capillary diffusion term:

$$\nabla \cdot \left(\rho \frac{Ks^3}{\mu} \frac{dP_c}{ds} \nabla s\right) = S_l \tag{8}$$

Table 2
Source terms in governing equations.

Source terms	Components	Expression
S_m	Anode CL	$-\frac{J_a}{2F} M_{H_2}$
	Cathode CL	$\frac{J_c}{2F} M_{H_2O} - \frac{J_c}{4F} M_{O_2}$
S_{mom}	GDL, CL	$-\frac{\mu^{eff} \varepsilon^2}{K} \vec{u}$
S_T	All	$I^2 R_{ohm} + h_{reaction} + \eta_{a,c} J_{a,c}$
S_i	Anode CL	$S_{H_2} = -\frac{J_a}{2F} M_{H_2}; S_{O_2} = -\frac{J_c}{4F} M_{O_2}$
	Cathode CL	$S_{H_2O} = \frac{J_c}{2F} M_{H_2O}$
S_{sol}, S_{mem}	Anode CL	$S_{sol} = -J_a; S_{mem} = -J_a$
	Cathode CL	$S_{sol} = J_c; S_{mem} = -J_c$
S_l	FC, GDL, CL	$S_l = \begin{cases} (1-s) c_r \frac{P_{wv} - P_{sat}}{RT} M_{H_2O}; & (P_{wv} > P_{sat}) \\ s c_r \frac{P_{wv} - P_{sat}}{RT} M_{H_2O}; & (P_{wv} < P_{sat}) \end{cases}$
S_α	Membrane	$S_\alpha = -\nabla \cdot \left(\frac{n_d}{F}\right)$

where K is permeability, s is water saturation and P_c represents capillary pressure.

Water conservation equation in membrane :

$$\nabla \cdot (D_\alpha \nabla \alpha) + S_\alpha = 0 \tag{9}$$

where S_α is the water content source term. The water content of the membrane, α, and the diffusion coefficient of the water content within the membrane, D_α, are determined by the following equations [39] :

$$\alpha = \begin{cases} 0.043 + 17.8a - 39.85a^2 + 36a^3; & 0 < a \le 1 \\ 14 + 1.4(a-1); & 1 < a \le 3 \end{cases} \tag{10}$$

$$D_\alpha = \begin{cases} 3.1 \times 10^{-7} \frac{\rho}{EW} \alpha \left(e^{0.28\alpha} - 1\right) \times e^{-2346/T}; & 0 < \alpha < 3 \\ 4.17 \times 10^{-8} \frac{\rho}{EW} \alpha (161 e^{-\alpha} + 1) \times e^{-2346/T}; & \text{otherwise} \end{cases} \tag{11}$$

where EW denotes equivalent molecular weight of electrolyte and the water activity a is calculated using :

$$a = \frac{C_w RT}{P_w^{sat}} \tag{12}$$

where C_w is water concentration, R is ideal gas constant and Psat w is saturation pressure of water.

The source terms in Eqs. (2)–(7) are listed in Table 2. Subscript a and c are anode and cathode, respectively. Further, the electro-osmotic drag coefficient in S_α, n^d, is determined by:

$$n^d = \frac{2.5\alpha}{22} \tag{13}$$

Table 3
Electrochemical parameters and operating conditions.

Parameter	Value
Operation pressure, Pa	101325
Operation temperature, K	343.15
Open circuit voltage, V	0.95
Anode stoichiometric ratio	3
Cathode stoichiometric ratio	3
Anode exchange coefficient	0.5
Cathode exchange coefficient	2
Anode concentration exponent	0.5
Cathode concentration exponent	1
Inlet relative humidity	100 %
Porosity of GDL	0.4
Porosity of CL	0.4
Absolute Permeability of GDL, m^{-2}	1.76×10^{-11}
Absolute Permeability of CL, m^{-2}	1.76×10^{-11}
Hydrogen reference diffusivity, m^2/s	9.15×10^{-5}
Oxygen reference diffusivity, m^2/s	2.2×10^{-5}
Anode exchange current density, A/m^3	1.4×10^{9}
Cathode exchange current density, A/m^3	2.0×10^{6}

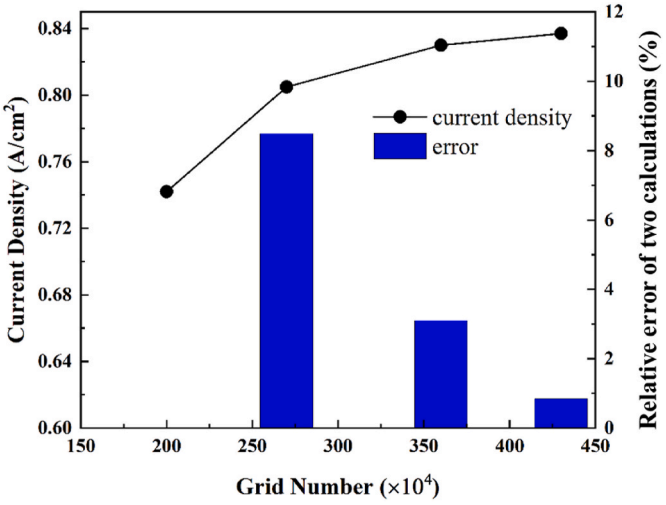

Fig. 4. Grid independence test.

2.3. Boundary conditions

The PEMFC add-on module in ANSYS fluent is used for the numerical simulation of this paper. The SIMPLE algorithm is applied to solve the pressure-velocity coupling, while the F-cycle method is used to improve the convergence speed of the calculation. The second-order difference scheme is used to discretize the momentum equation, while a second-order upwind scheme is applied to discretize the species conservation equation and the charge conservation equation. In the simulation, the flow channel outlets are set to the pressure outlet boundary and they are equal to the operating pressure. Both the anode and cathode inlets are set as mass-flow inlets and fed with fully humidified hydrogen and air, respectively. The mass-flow rates at the anode and cathode are calculated using the following equations:

$$Q_a = A_{mem}\frac{\zeta_a M_{H_2} I^{ref}}{2FY_{H_2}} \tag{14}$$

$$Q_c = A_{mem}\frac{\zeta_c M_{O_2} I^{ref}}{4FY_{O_2}} \tag{15}$$

where Q, A_{mem} and ζ are mass flow rate, membrane area, and stoichiometric ratio, respectively. I^{ref} is the reference current density. All solid surfaces are set to no-slip boundary conditions. For the electron potential equation, the anode BP upper boundary is set to 0 while the cathode BP lower boundary is fixed to the operating voltage. The main electrochemical parameters and operating conditions are listed in Table 3.

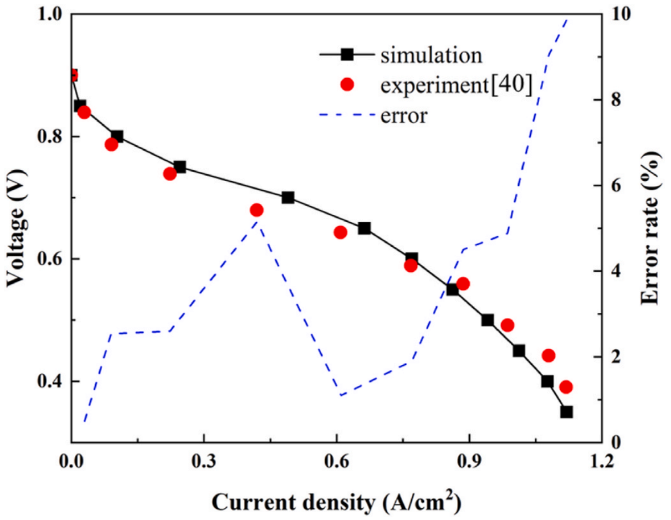

Fig. 5. Comparison of the polarization curves between the numerical results and experiment data [40].

2.4. Grid independence test and model validation

To assess grid independence, five sets with different numbers of grids were created, and their current densities at 0.55 V were calculated. As shown in Fig. 4, the difference between the results calculated using 4.3 million grids and those using 3.6 million grids is only 1 %. Considering the simulation accuracy and computational cost, models with 3.6 million grids were used for the simulations conducted in this study.

In addition, comparison with experimental data can further verify the reliability of the numerical model employed in this study [34,37]. Therefore, a numerical model of a single-channel PEMFC with dimensions consistent with Ref. [40] was established and compared with experimental data [40], as illustrated in Fig. 5. The channel length and width were 70 mm and 1 mm. The operating temperature of the PEMFC is 343 K and the operating pressure is 1 atm. At high current densities, the relative error in voltage is large due to the low voltage value, but the maximum error is still less than 10 %, so the PEMFC model developed in this paper meets the requirement of calculation accuracy.

3. Optimization process

Fig. 6 outlines the flowchart for the optimal design approach, which combines computational fluid dynamics (CFDs), an ANN, and a PSO algorithm. In this study, we investigated the collective impact of under-rib channels and GDL gradient porosity on PEMFC performance while keeping other variables constant. To minimize simulation costs and maximize the informational value of limited data, LHS was employed to design the sampling points. These points were then geometrically modeled, meshed, and numerically evaluated to obtain a series of corresponding output power values. This obtained data was used to train the ANN, creating a fitting function that maps input parameters to output performance. The optimal parameters were subsequently identified using the PSO algorithm.

3.1. Definition of input variables and optimization objective

To improve output performance of PEMFC, the four structural parameters, N, H, W, k, in Figs. 2 and 3 were extracted, and the selection range of the variables are determined as follows：

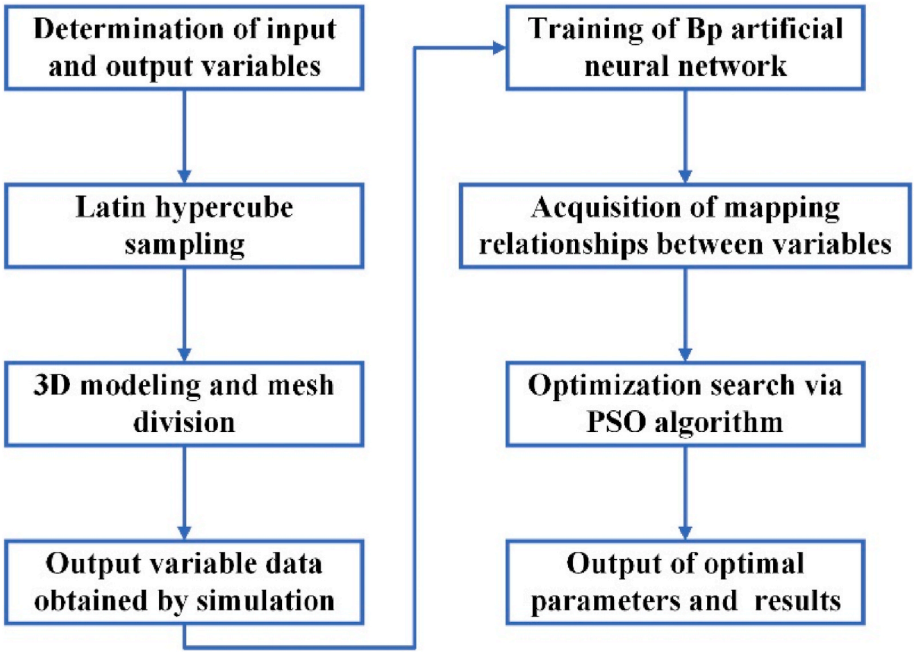

Fig. 6. Flowchart for coupled optimization.

$$\begin{aligned} 4 \le N \le 10 \\ 0.1\text{mm} \le H \le 0.9\text{mm} \\ 0.2\text{mm} \le W \le 1.5\text{mm} \\ 0 \le k \le 3.2 \end{aligned} \tag{16}$$

The maximum output power density, P_{max}, is one of the most important indicators for evaluating the PEMFC output performance; therefore, P_{max} is used as the optimization objective function.

3.2. Latin hypercube sampling

LHS is a stratified sampling technique that enables near-random sampling from multivariate parameters. It significantly reduces the number of required samples while ensuring they span the entire range of variable distributions [41]. The LHS process involves the following steps:

1) Determine the parameters to be sampled and the range of values to be taken.
2) Divide the value space for each parameter into 'n' parts, each having an equal probability of selection, as illustrated in Fig. 7(a) (b), where F(x) is probability distribution function, P(x) is probability density function, and xi is the value of the independent variable.
3) For each parameter, randomly select one value from each part of the value space.
4) Combine these randomly selected values with those from other parameters to form a vector, serving as a sample point. Repeat this 'n' times to generate 'n' sample points.

To provide a practical example, Fig. 7(c) outlines the LHS procedure of two parameters, X and Y. Here, samples are drawn from each segment of the value space for every parameter. Once a value is selected from a segment, that particular segment is no longer considered for additional sampling.

In this study, given the number and range of the four selected parameters, 280 sampling points were designed using LHS. These sampling points were then employed for geometric modeling, meshing, and numerical simulations, focusing on optimizing the P_{max}. The computational data obtained from these simulations were subsequently used to train the ANN model.

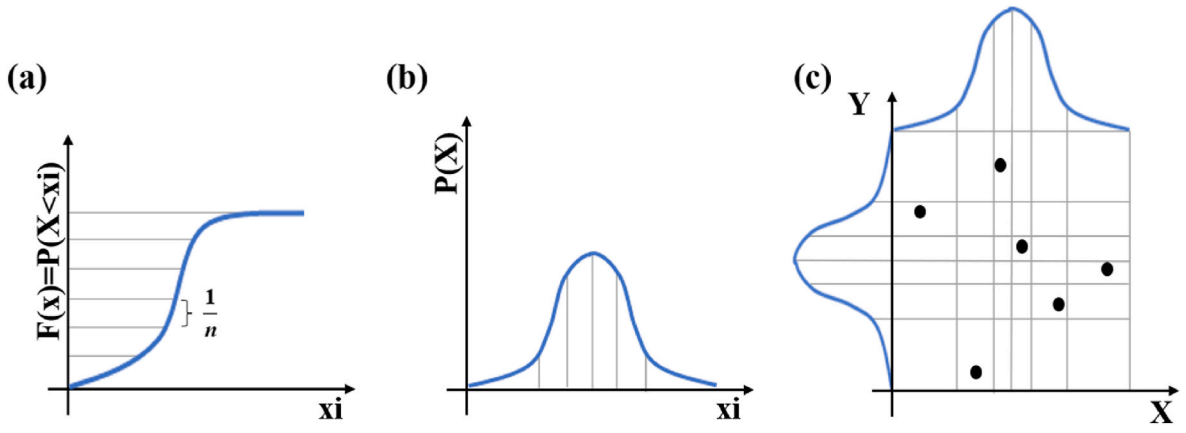

Fig. 7. LHS of two parameters (a) probability density function, (b)cumulative distribution function, (c) distribution of sampling points.

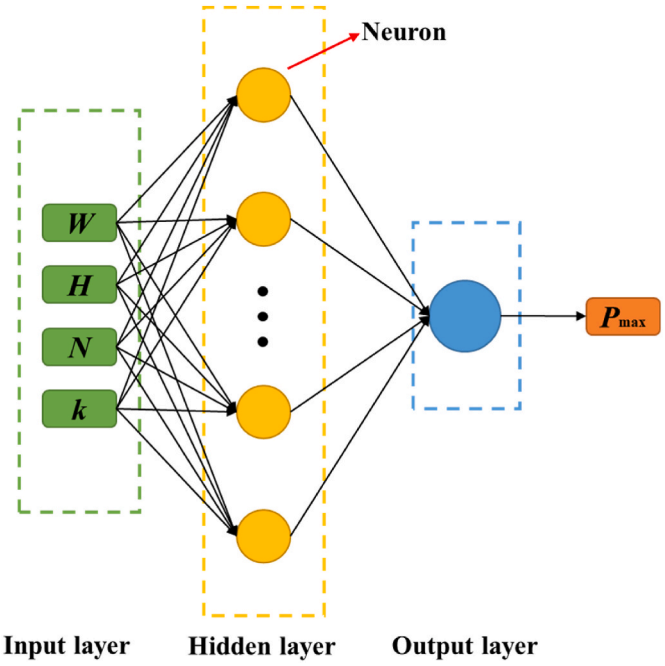

Fig. 8. Structure of BP neural network.

3.3. Artificial neural network surrogate model

An ANN is an arithmetic model consisting of a large number of interconnected neurons, designed to emulate the neural networks found in human brain, from the perspective of information processing and forms different networks according to different connections [42]. By adjusting the neuron weights through continuous training, ANNs can closely approximate real-world data, enabling them to analyze complex relationships between variables and effectively map input to output. The BP neural network is established by MATLAB, which consists of an input layer, a hidden layer, and an output layer, as shown in Fig. 8. Data fed into the input layer undergo processing in the hidden layer before reaching the output layer. Here, the error between the actual and predicted output is calculated and passed back to adjust the neuron weights in the hidden layer. In this study, we employed the Levenberg–Marquardt BP algorithm for training the ANN. The number of neurons in hidden layer was 10 and the maximum number of iterations is 1000. The dataset was randomly segmented into three subsets: 70 % for training, and 15 % each for validation and test. If the error cannot be reduced for eight consecutive training sessions, the training is terminated.

Fig. 9 demonstrates the performance of ANN model for PEMFC optimization. The performance of ANN in predicting output variables is evaluated using the regression coefficient (R) and the mean square error (MSE). A regression coefficient close to 1 and a low MSE indicate high accuracy in the predictions of ANN. For each dataset, R is greater than 0.999 and MSE is less than 1e-6, affirming the high predictive accuracy of ANN.

3.4. Particle swarm optimization algorithm

With the ANN model obtained above, the mapping relationship between the input parameters and the objective function can be obtained. To identify the optimal combination of the four input variables, we integrated PSO algorithm with the ANN model. PSO is renowned for its high accuracy, fast convergence, and ease of implementation. It

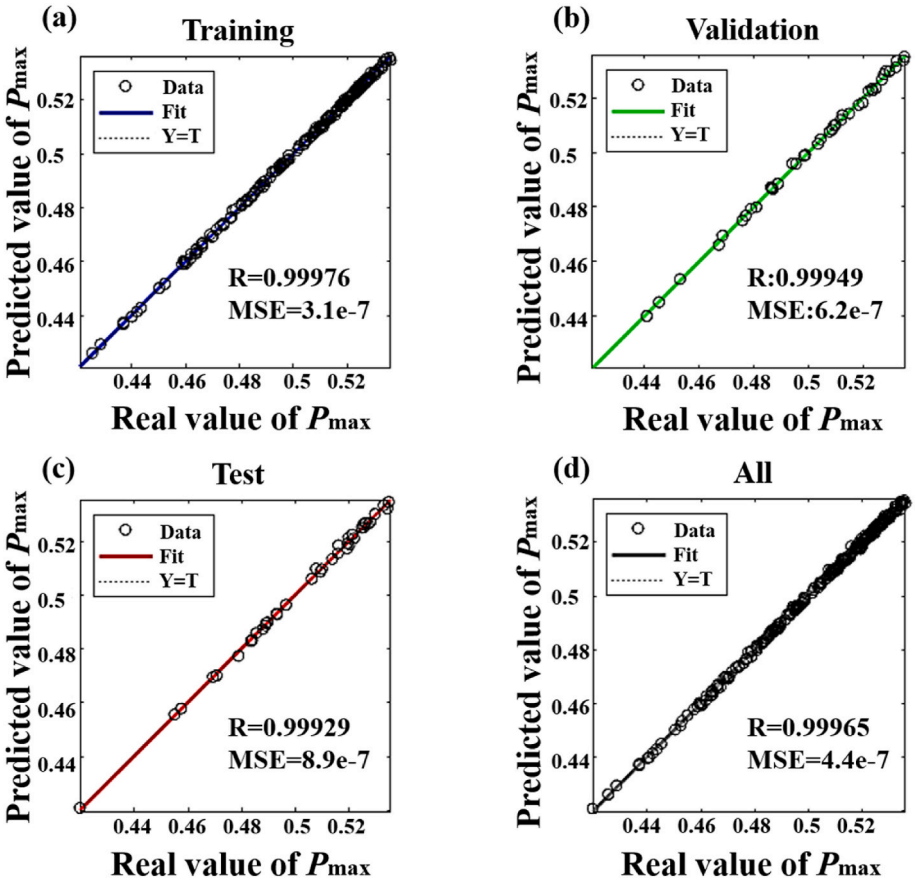

Fig. 9. Prediction performance of ANN for subsets of (a) training, (b) validation, (c) test, (d) all.

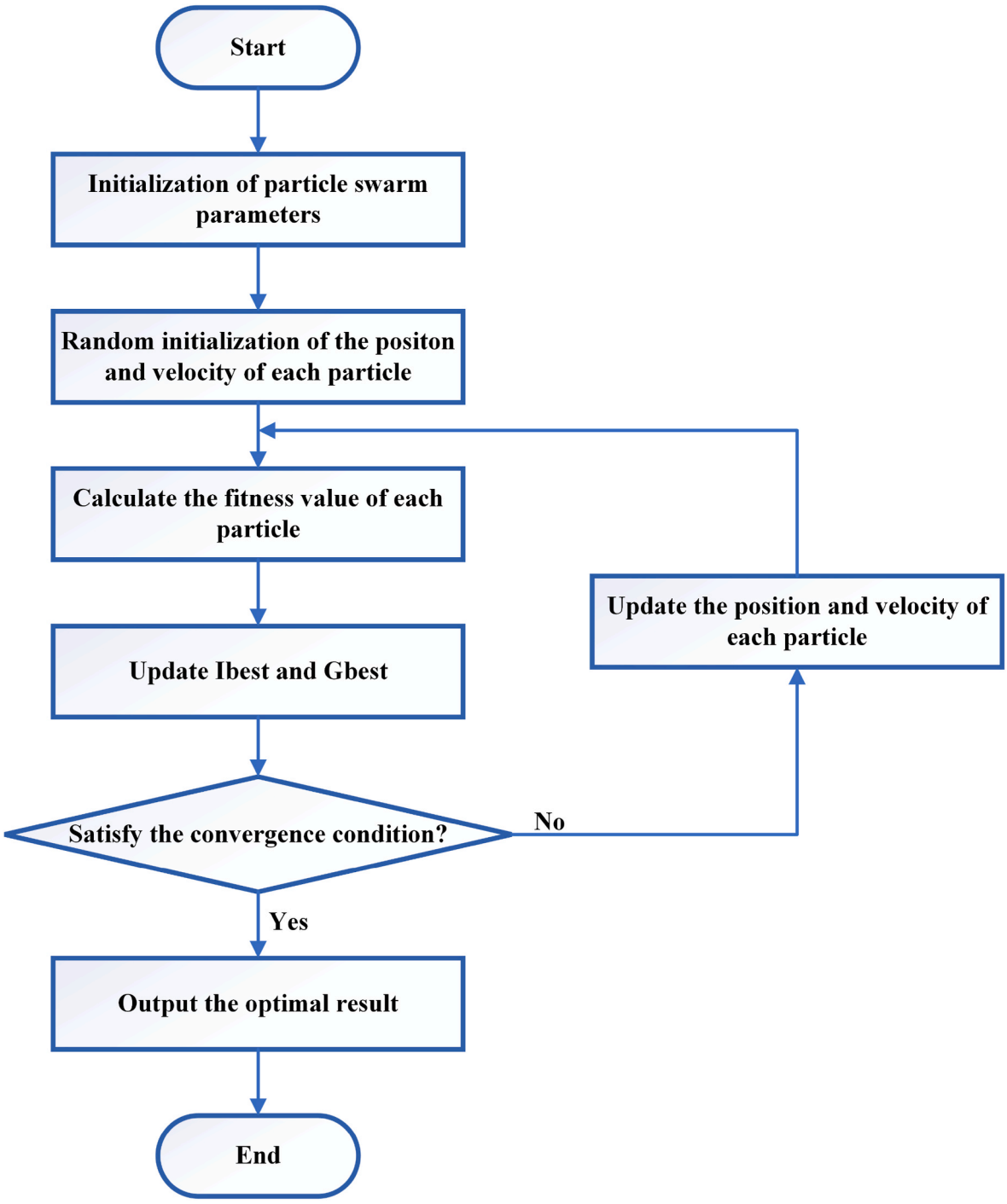

Fig. 10. Computational flowchart for PSO of PEMFC optimization.

simulates the foraging behavior of a flock of birds, representing each bird as a particle characterized by two parameters: velocity and position.

Table 4
Optimal parameters of COPFF and output results.

Optimization results	value
N	8
W, mm	0.3977
H, mm	0.4778
k	2.2435
Predicted power density, W/cm^2	0.5354
Simulated power density, W/cm^2	0.5357

Here, velocity indicates the direction and distance the particle will move in the next iteration, while position denotes a potential solution.

In the ith iteration, the position of a particle in n-dimensional space is represented by the vector $\boldsymbol{X}_i=(x_1, x_2 \ldots x_n)$, and its velocity is represented by $\boldsymbol{V}_i=(v_1, v_2 \ldots v_n)$. The best solution obtained by each particle is $\boldsymbol{Ibest}_i$, while $\boldsymbol{Gbest}_i$ represents the global optimal solution across the whole particle swarm search. Each particle adjusts its velocity and position based on $\boldsymbol{Ibest}_i$ and $\boldsymbol{Gbest}_i$, with Eqs. (17) and (18):

$$\boldsymbol{V}_{i+1} = w \cdot \boldsymbol{V}_i + c_1 \times r_1 \times (\boldsymbol{Ibest}_i - \boldsymbol{X}_i) + c_2 \times r_2 \times (\boldsymbol{Gbest}_i - \boldsymbol{X}_i) \quad (17)$$

$$\boldsymbol{X}_{i+1} = \boldsymbol{X}_i + \boldsymbol{V}_{i+1} \quad (18)$$

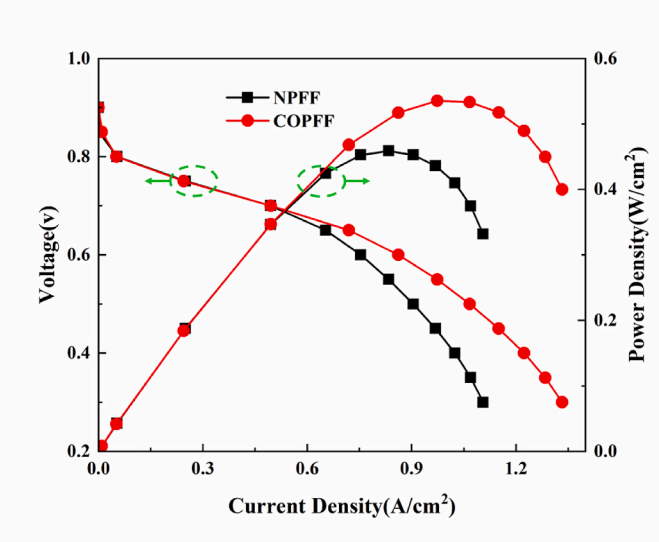

Fig. 11. Polarization curves and power curves of the COPFF and NPFF.

where, the parameters w denotes the inertia factor, c_1 and c_2 represent the individual and global learning factor, respectively, while r_1 *and* r_2 are random numbers between 0 and 1. The computational flowchart for PSO is depicted in Fig. 10.

In this study, the size of the particle population was set to 2000, the maximum number of iterations was 500, and the maximum velocity of the particle motion was 5 % of the variable range. The optimal parameters and optimal output power density are obtained by PSO and numerically verified by CFD. The results are then listed in Table 4, and the relative error between the predicted and simulated power densities was only 0.05 %, which further proves the validity of the surrogate model.

4. Results and discussion

4.1. Performance analysis of COPFF and NPFF

Polarization and power curves serve as crucial metrics for assessing the performance of PEMFCs. Fig. 11 presents the output performances for both the COPFF and NPFF PEMFCs. While there is negligible difference in output performance at low current densities, the COPFF significantly outperforms the NPFF at medium to high current densities. This is due to the fact that at low current densities, the irreversible losses in the PEMFC come mainly from activation polarization and ohmic polarization, which are mainly affected by the nature of the catalyst and the internal resistance of the cell. However, with the increase of current density, the electrochemical reaction becomes more and more intense, and the concentration polarization caused by the insufficient mass transfer capacity at the cathode side gradually becomes the main source of irreversible loss, at this time, improving the mass transfer capacity of the cell is an effective way to improve the performance of the cell. Specifically, at a voltage of 0.55 V, where both configurations reach their maximum output power, the COPFF registers 0.5356 W/cm^2, which is 16.7 % higher than the NPFF's 0.4588 W/cm^2. Moreover, at 0.3 V, the current density for the COPFF (1.3329 A/cm^2) is 20.6 % higher than that for the NPFF (1.1056 A/cm^2). These findings suggest that strategically designed under-rib auxiliary channels and a gradient in GDL porosity can substantially elevate the maximum output power and broaden the current operating range of the PEMFC.

Facilitating the diffusion of reactants from the FC to the CL is a key function of the GDL, making the distribution of each species within the GDL an important indicator for evaluating a cell's mass-transfer performance. Fig. 12(a) displays the oxygen concentration distribution in the cathode GDL at 0.55 V. The COPFF exhibits both higher and more uniform oxygen concentration compared to the NPFF, reflecting the significant superiority of COPFF in terms of mass transfer capacity. The average oxygen mass fraction of COPFF is 0.076, which is 33.3 % higher than NPFF's 0.057.

Fig. 12(b) depicts the water saturation distribution in the intermediate sections of GDLs of NPFF and COPFF at the same voltage. The average liquid saturation of NPFF is 0.157 while that of COPFF is 0.112. The NPFF has notably higher water saturation, particularly toward the end of the flow field where liquid water accumulates significantly, reaching saturation levels as high as 0.17. In contrast, the COPFF maintains lower water saturation, peaking at just 0.13, which is a reduction of 23.5 %, indicating superior water-removal performance. In addition, water saturation tends to increase along the flow direction due to the accumulation of liquid water. However, a region of low water saturation exists in the middle and lower parts of the cell. This is due to low oxygen concentration, which results in an insufficient electrochemical reaction and consequently lesser water production.

As shown in Fig. 12(c), the current density distribution in the middle cross section of the CLs on the cathode side of the NPFF and COPFF PEMFC was carried out to study whether the PEMFC active area was effectively utilized. It can be found that the current density of COPFF is clearly higher than that of NPFF. In addition, combined with Fig. 12(a), it can be seen that the distribution of current density is similar to that of oxygen concentration. The region below the rib is less capable of mass transfer and has insufficient oxygen content, so the electrochemistry is less intense and the current density is lower. However, the COPFF PEMFC improves the output performance via a better oxygen mass transfer performance.

Fig. 13 illustrates the gas motion trajectories within the cathodic flow fields for both the NPFF and COPFF configurations. Gas flow velocity in the COPFF is notably higher compared to the NPFF. Additionally, the presence of auxiliary channels between adjacent flow paths enables the gas to separate and recombine continuously, leading to a more even distribution of gas. Due to factors such as pressure differential and wall effects, the last four FCs in both NPFF and COPFF configurations exhibit the highest flow velocities. These are followed by the initial three channels, with the middle three channels showing the slowest velocities. This flow velocity distribution also leads to a region of low oxygen concentration associated with the middle and bottom of the two flow fields, as depicted in Fig. 12(a).

4.2. Coupling effects of under-rib auxiliary channels and GDL porosity gradient

To evaluate the effects of auxiliary channels and GDL gradient porosity on cell performance, we developed two distinct configurations for comparison: a parallel-flow-field PEMFC with GDL gradient porosity (GPPFF) and an auxiliary-channel parallel-flow-field PEMFC (ACPFF). Both configurations obtain the same optimized structural parameters from the COPFF PEMFC. When examined alongside the data in Fig. 14, it is evident that the GPPFF enhances the maximum power to 0.4877 W/cm^2, a 6.3 % increase, and the maximum current density to 1.145 A/cm^2, a 3.6 % increase, compared to the NPFF. Meanwhile, the ACPFF achieves a maximum power of 0.4928 W/cm^2 and a maximum current density of 1.222 A/cm^2, reflecting increases of 7.4 % and 10.6 %, respectively. In comparison to the GPPFF, the ACPFF does not display a significant difference in performance at low and medium current densities. However, it outperforms the GPPFF at high current densities. Obviously, NPFF as the standard of comparison, the performance improvements offered by the COPFF (16.7 % in the maximum power density and 20.6 % in the maximum current density) exceed the benefits of both the GPPFF and ACPFF at medium to high current densities. This suggests a mutually reinforcing effect between the auxiliary channels and the GDL porosity gradient, the underlying mechanisms of which will be explored later in combination with species distribution contours.

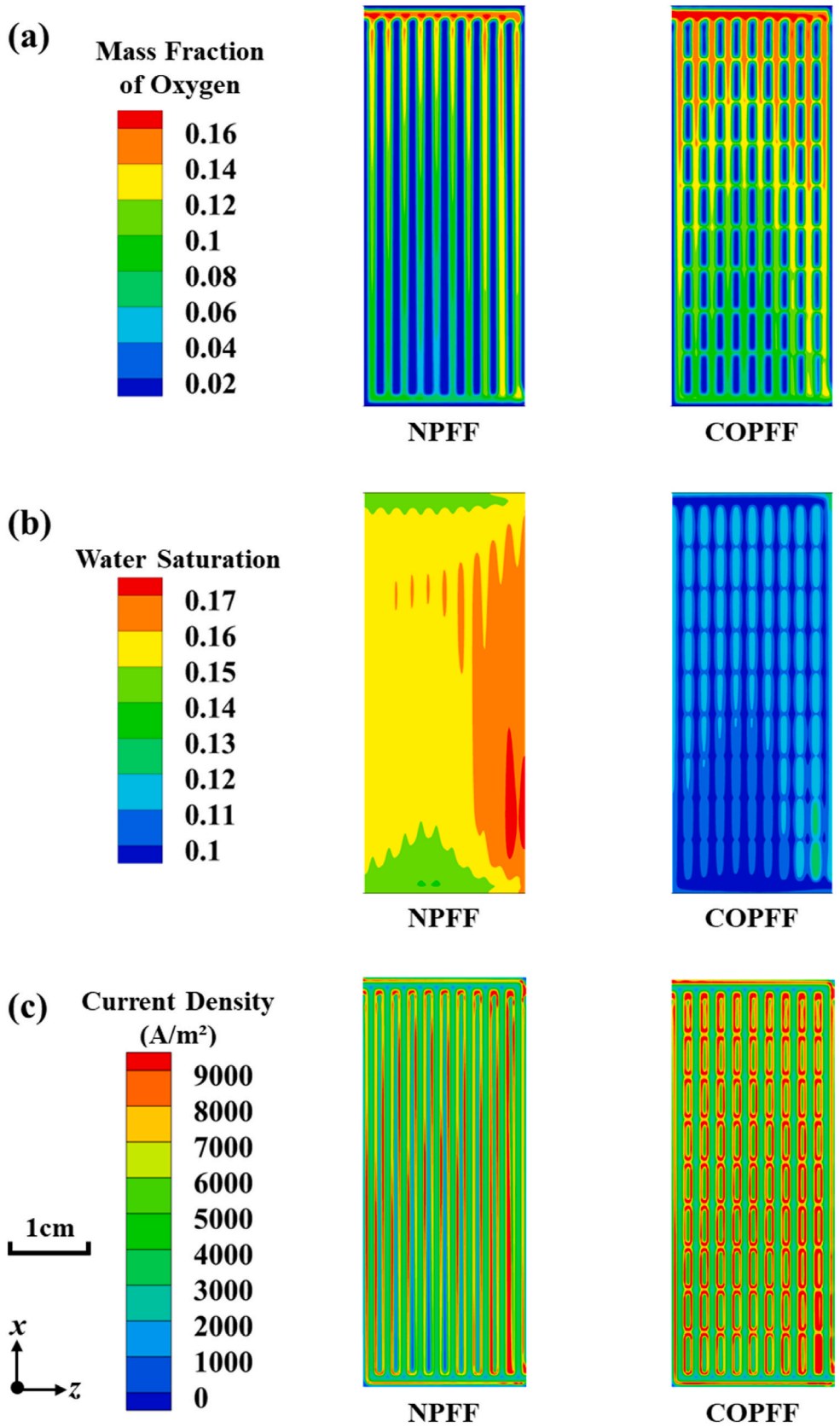

Fig. 12. At 0.55 V, (a) Oxygen concentration distribution in the intermediate sections of GDLs, (b) water saturation distribution in the intermediate sections of GDLs and (c) current density distribution in the intermediate sections of CLs of the NPFF and COPFF.

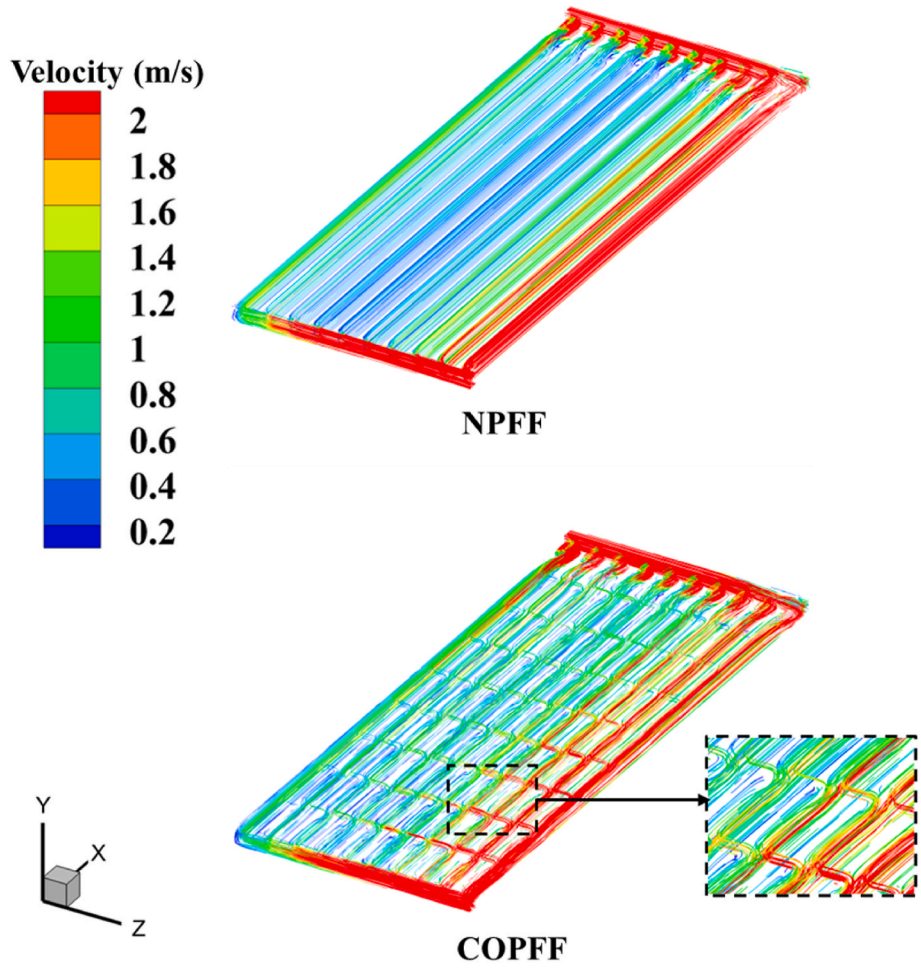

Fig. 13. Reaction gas flow traces of cathode flow field of NPFF and COPFF.

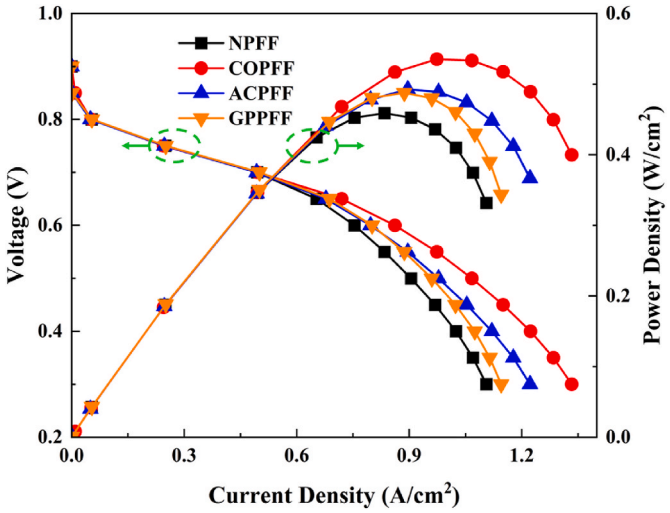

Fig. 14. Polarization curves and power curves of the GPPFF and ACPFF.

The oxygen concentration profiles in the intermediate sections of GDLs for the GPPFF and ACPFF cathode at 0.55 V are illustrated in Fig. 15(a). The average mass fraction of oxygen of GPPFF is 0.063 while that of ACPFF is 0.070. When integrated with the data from Fig. 12(a), it is evident that the oxygen mass fraction of GPPFF was slightly higher than that of NPFF (0.057), whereas the oxygen content of ACPFF was higher than that of GPPFF. This indicates that the auxiliary channels significantly improve the mass transfer capacity of the cell, thus increasing the oxygen levels and enhancing their uniform distribution, while the improvement of porosity gradient is not as pronounced as that of the auxiliary channels. In other words, enhanced oxygen transport is largely independent of porosity type and is driven by enhanced gas mixing and increased transfer area offered by the under-rib auxiliary channels.

Fig. 15(b) presents the water saturation profiles in the intermediate sections of GDLs of GPPFF and ACPFF. The average liquid saturation of GPPFF is 0.154 and that of ACPFF is 0.164. When compared with Fig. 12 (b), it is clear that the ACPFF has the highest water saturation among all configurations. This is attributable to enhanced oxygen transport, which amplifies the electrochemical reactions, thereby leading to greater water production. In contrast, both the GPPFF and COPFF have lower water saturation compared to the NPFF, indicating enhanced water-removal capabilities. This feature arises not from the under-rib channels, but from the gradient porosity, which creates higher capillary pressure differentials in the GDL, facilitating easier water discharge. As a result, a larger pore area becomes available for oxygen transport, explaining why gradient porosity can positively impact oxygen distribution within the GDL. In addition, this is the reason that the COPFF significantly outperforms the GPPFF and ACPFF at medium to high current densities, shown in Fig. 14. The synergy between the auxiliary channel and the GDL porosity gradient can be explained in this way: the channel facilitates a better transport of oxygen, which enhances the electrochemical reaction and consequently the production of more water, and at this point, when the benefit of the gradient porosity for water removal

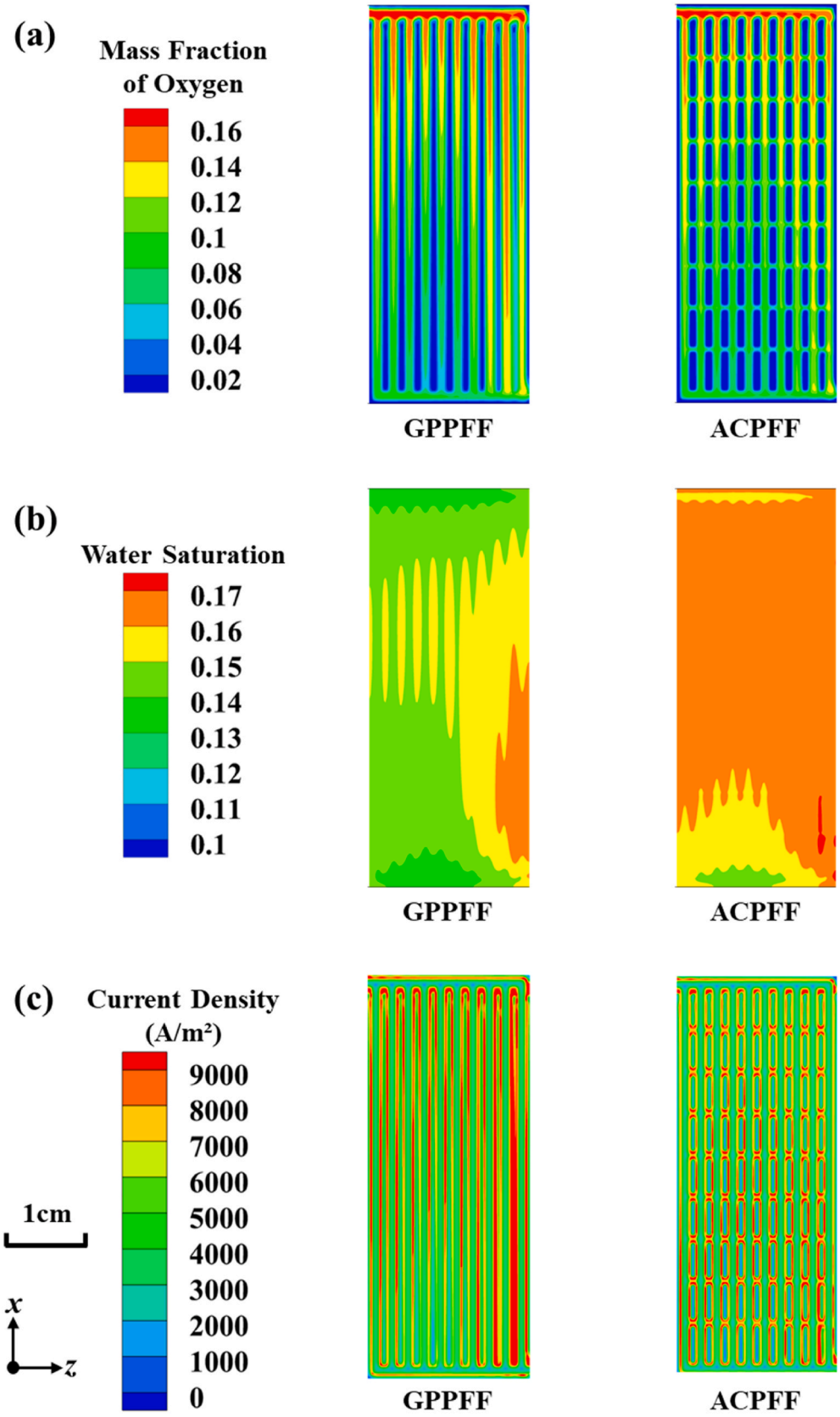

Fig. 15. At 0.55 V, (a) Oxygen concentration distribution in the intermediate sections of GDLs, (b) water saturation distribution in the intermediate sections of GDLs and (c) current density distribution in the intermediate sections of CLs of the GPPFF and ACPFF.

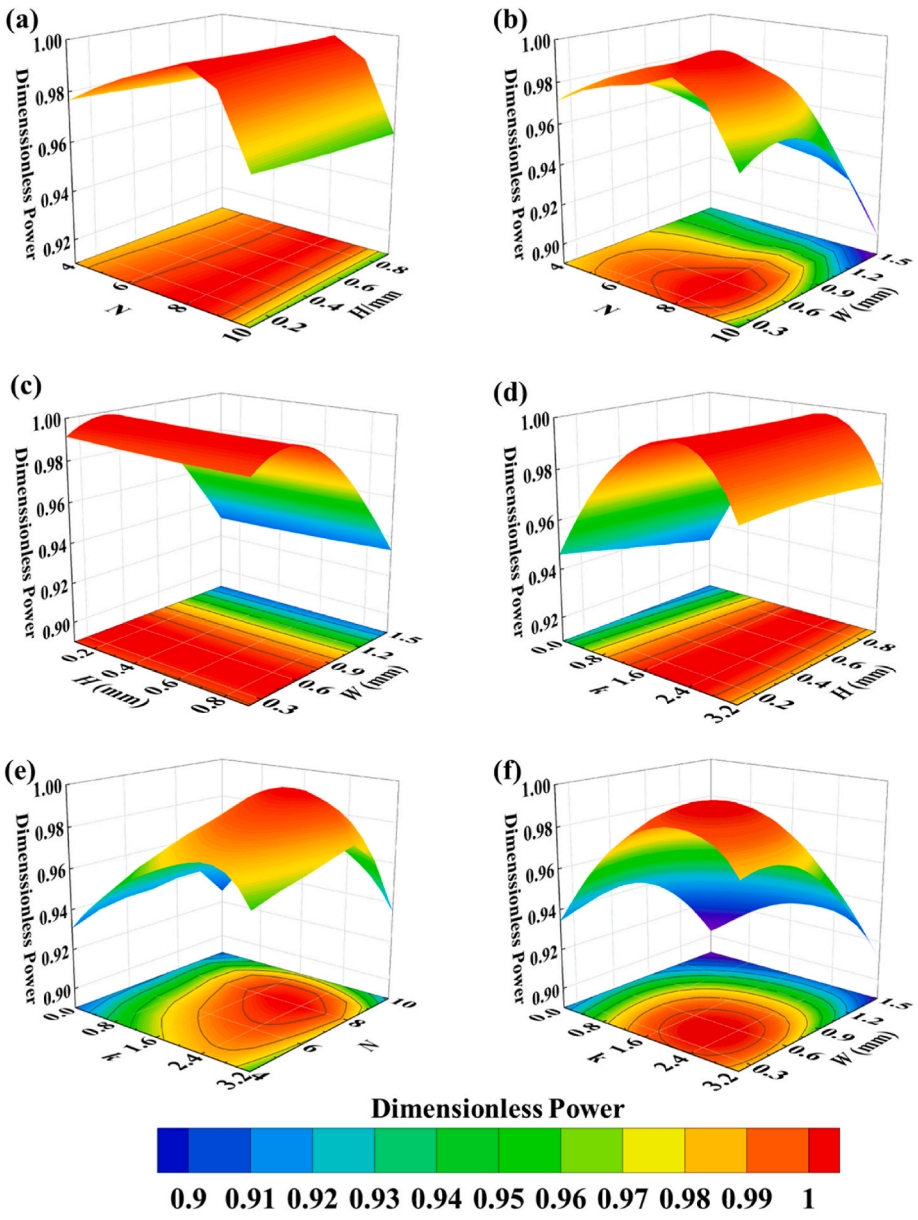

Fig. 16. Interaction effects of different parameters on dimensionless power (a) *N* and *H*, (b) *N* and *W*, (c) *H* and *W*, (d) *k* and *H*, (e) *k* and *N*, (f) *k* and *W*.

becomes more and more important, the interaction between these two elements culminates in further performance improvements for the cell.

The current density distribution in the middle cross section of the catalyst layer for ACPFF and GPPFF is given in Fig. 15(c). Combined with Fig. 12(c), it can be seen that the optimization of individual components significantly improves the current density within the catalyst layer compared to NPFF, but none of the improvements are as good as COPFF. Besides, the similarity of the current density and oxygen concentration distributions further validates the improvement of the output performance by the increase in mass transfer.

Finally, we investigate the interactive effects of the four input parameters, the number of auxiliary channels under a rib (*N*), the height of the auxiliary channels (*H*), the height of the auxiliary channels (*W*) and the GDL porosity gradient (*k*), on cell performance by response surface analysis. Fig. 16 shows the response surface plots of the dimensionless power versus all combinations consisting of two parameters.

As shown in Fig. 16(a), (c), and (d), there is almost no interaction between the variation of *H* and *N*, *W*, or *k* and it has the least effect on the output performance of the cell. With all other parameters remaining constant, the maximum difference in output power for different *H* is only 0.6 %. Fig. 16(b), (e), and (f) demonstrate the effects of *N*, *W*, and *k* on output performance. Each figure shows a set of parameter combinations that can achieve the maximum output power of the cell; the farther the parameters deviate from this optimal combination, the more the output power will decrease. The results indicate that variations in *k* and *W* may lead to a large variation in the dimensionless power, which can seriously affect the output performance of PEMFC. Even if the other parameters are kept at optimal values, unreasonable *k* and *W* may lead to maximum output power losses of 5.9 % and 6.5 %, respectively. Besides, the effect of *N* is relatively small and may result in a power loss of 3.6 %. Therefore, a larger number of auxiliary channels and narrower widths are more favorable for improving the output performance of the cell, while a GDL porosity gradient that is either too large or too small diminishes the output power. This again demonstrates the necessity and effectiveness of simultaneously optimizing the flow channel and GDL structure.

5. Conclusions and outlook

In this study, we introduce a novel under-rib auxiliary channel and develop an optimization method that combines computational fluid dynamics, artificial neural network, and particle swarm optimization algorithm. This approach aims to simultaneously optimize the auxiliary channel structures and gas diffusion layer porosity gradient and investigate the coupled effect of two components optimization on the output performance and mass-transfer capacity of proton exchange membrane fuel cell. The following conclusions are obtained:

1) The optimization framework, integrating computational fluid dynamics and artificial neural network, can establish the relationship between input structural parameters and the output power density, significantly enhancing computational efficiency.
2) Under-rib channels and gas diffusion layers porosity gradient markedly improve PEMFC's output performance. In comparison to the original cell, the coupled optimized cell exhibits substantial gains: a 16.7 % increase in maximum output power and a 20.6 % expansion in current density range.
3) Under-rib channels facilitate continuous separation and recombination of reactants between adjacent gas flow channels. This architecture effectively improves the mass-transfer performance of the cell, boosts oxygen transfer, and optimizes distribution uniformity.
4) Gradient porosity in the cathode gas diffusion layer amplifies the water-removal capacity of the cell. This, in turn, frees up more pore space for oxygen transfer, bolstering both mass transfer and output capacity.
5) A synergistic interaction exists between the benefits conferred by under-rib channels and gas diffusion layer porosity gradient. While optimizing each factor individually can enhance cell performance, the gains from combined optimization are significantly greater.

This paper is limited by computation load and still has some regrets. In the future, we could consider applying the optimization method to commercial cells to obtain better application prospects. In addition, according to the conclusion of this paper, optimizing a single component cannot obtain the optimal output performance. The cell performance depends on the matching of the operating and structural parameters of all components. Therefore, we could extend the optimized components to the anode flow channel, anode gas diffusion layer, and even catalyst layers to achieve the systematic optimization of a whole proton exchange membrane fuel cell.

CRediT authorship contribution statement

Cong Tian: Writing – original draft, Visualization, Investigation, Data curation. **Fang Yuan:** Writing – review & editing, Resources, Formal analysis, Conceptualization. **Tianlun Deng:** Writing – review & editing, Validation. **Qianhui He:** Writing – review & editing, Validation. **Cen Hu:** Writing – review & editing, Validation. **Yong Chen:** Writing – review & editing, Methodology. **Wei Liu:** Writing – review & editing, Conceptualization.

Declaration of competing interest

The authors declare that they have no known competing financial interests or personal relationships that could have appeared to influence the work reported in this paper.

Data availability

Data will be made available on request.

References

[1] Fan L, Tu Z, Chan SH. Recent development of hydrogen and fuel cell technologies: a review. Energy Rep 2021;7:8421–46.
[2] Hwang J, Maharjan K, Cho H. A review of hydrogen utilization in power generation and transportation sectors: achievements and future challenges. Int J Hydrogen Energy 2023;48(74):28629–48.
[3] Li M, Bai Y, Zhang C, Song Y, Jiang S, Grouset D, et al. Review on the research of hydrogen storage system fast refueling in fuel cell vehicle. Int J Hydrogen Energy 2019;44(21):10677–93.
[4] Lü X, Qu Y, Wang Y, Qin C, Liu G. A comprehensive review on hybrid power system for PEMFC-HEV: issues and strategies. Energy Convers Manag 2018;171:1273–91.
[5] Meda US, Rajyaguru YV, Pandey A. Generation of green hydrogen using self-sustained regenerative fuel cells: opportunities and challenges. Int J Hydrogen Energy 2023;48(73):28289–314.
[6] Cai Y, Wu D, Sun J, Chen B. The effect of cathode channel blockages on the enhanced mass transfer and performance of PEMFC. Energy 2021;222.
[7] Ijaodola OS, El- Hassan Z, Ogungbemi E, Khatib FN, Wilberforce T, Thompson J, et al. Energy efficiency improvements by investigating the water flooding management on proton exchange membrane fuel cell (PEMFC). Energy 2019;179:246–67.
[8] Shimpalee S, Beuscher U, Van Zee JW. Analysis of GDL flooding effects on PEMFC performance. Electrochim Acta 2007;52(24):6748–54.
[9] Ahmed DH, Sung HJ. Effects of channel geometrical configuration and shoulder width on PEMFC performance at high current density. J Power Sources 2006;162(1):327–39.
[10] Li X, Sabir I. Review of bipolar plates in PEM fuel cells: flow-field designs. Int J Hydrogen Energy 2005;30(4):359–71.
[11] Chiu H-C, Jang J-H, Yan W-M, Li H-Y, Liao C-C. A three-dimensional modeling of transport phenomena of proton exchange membrane fuel cells with various flow fields. Appl Energy 2012;96:359–70.
[12] Zhou Y, Chen B, Chen W, Deng Q, Shen J, Tu Z. A novel opposite sinusoidal wave flow channel for performance enhancement of proton exchange membrane fuel cell. Energy 2022;261.
[13] Wan Z, Quan W, Yang C, Yan H, Chen X, Huang T, et al. Optimal design of a novel M-like channel in bipolar plates of proton exchange membrane fuel cell based on minimum entropy generation. Energy Convers Manag 2020;205.
[14] Zuo Q, Li Q, Chen W, Peng R, Zhu X, Xie Y, et al. Optimization of blocked flow field performance of proton exchange membrane fuel cell with auxiliary channels. Int J Hydrogen Energy 2022;47(94):39943–60.
[15] Liao S, Qiu D, Yi P, Peng L, Lai X. Modeling of a novel cathode flow field design with optimized sub-channels to improve drainage for proton exchange membrane fuel cells. Energy 2022;261.
[16] Perng S-W, Wu H-W, Shih G-J. Effect of prominent gas diffusion layer (GDL) on non-isothermal transport characteristics and cell performance of a proton exchange membrane fuel cell (PEMFC). Energy 2015;88:126–38.
[17] Xu S, Liao P, Yang D, Li Z, Li B, Ming P, et al. Liquid water transport in gas flow channels of PEMFCs: a review on numerical simulations and visualization experiments. Int J Hydrogen Energy 2023;48(27):10118–43.
[18] Zhang M, Yu M, Liu Z, Tu Z, Liu W. Moisture migration in the cathode GDL of PEMFC under variable physical parameters based on a modified two-fluid model. Int J Hydrogen Energy 2023;48(41):15657–76.
[19] Chien C-H, Hu Y-L, Su T-H, Liu H-T, Wang C-T, Yang P-F, et al. Effects of bolt pre-loading variations on performance of GDL in a bolted PEMFC by 3-D FEM analysis. Energy 2016;113:1174–87.
[20] Xia L, Ni M, He Q, Xu Q, Cheng C. Optimization of gas diffusion layer in high temperature PEMFC with the focuses on thickness and porosity. Appl Energy 2021;300.
[21] Yin B, Xu S, Yang S, Dong F. Influence of microelliptical groove gas diffusion layer (GDL) on transport behavior of proton exchange membrane fuel cell (PEMFC). Int J Heat Mass Tran 2021;180.
[22] Li Y, Yuan F, Weng R, Xi F, Liu W. Variational-principle-optimized porosity distribution in gas diffusion layer of high-temperature PEM fuel cells. Energy 2021;235.
[23] Ko D, Doh S, Park HS, Kim MH. The effect of through plane pore gradient GDL on the water distribution of PEMFC. Int J Hydrogen Energy 2018;43(4):2369–80.
[24] Shangguan X, Li Y, Qin Y, Cao S, Zhang J, Yin Y. Effect of the porosity distribution on the liquid water transport in the gas diffusion layer of PEMFC. Electrochim Acta 2021;371.
[25] Zhang S-y, Qu Z-g, Xu H-t, Talkhoncheh F-K, Liu S, Gao Q. A numerical study on the performance of PEMFC with wedge-shaped fins in the cathode channel. Int J Hydrogen Energy 2021;46(54):27700–8.
[26] Xu C, Wang H, Cheng T. Wave-shaped flow channel design and optimization of PEMFCs with a groove in the gas diffusion layer. Int J Hydrogen Energy 2023;48(11):4418–29.
[27] Liu Z, Zeng X, Ge Y, Shen J, Liu W. Multi-objective optimization of operating conditions and channel structure for a proton exchange membrane fuel cell. Int J Heat Mass Tran 2017;111:289–98.
[28] Tan J, Hu H, Liu S, Chen C, Xuan D. Optimization of PEMFC system operating conditions based on neural network and PSO to achieve the best system performance. Int J Hydrogen Energy 2022;47(84):35790–809.
[29] Zeng X, Ge Y, Shen J, Zeng L, Liu Z, Liu W. The optimization of channels for a proton exchange membrane fuel cell applying genetic algorithm. Int J Heat Mass Tran 2017;105:81–9.
[30] Cai G, Liang Y, Liu Z, Liu W. Design and optimization of bio-inspired wave-like channel for a PEM fuel cell applying genetic algorithm. Energy 2020;192.

[31] Liu S, Tan J, Hu H, Lu C, Xuan D. Multi-objective optimization of proton exchange membrane fuel cell geometry and operating parameters based on three new performance evaluation indexes. Energy Convers Manag 2023;277.
[32] Feng S, Huang W, Huang Z, Jian Q. Optimization of maximum power density output for proton exchange membrane fuel cell based on a data-driven surrogate model. Appl Energy 2022;317.
[33] Wilberforce T, Olabi AG, Rezk H, Abdelaziz AY, Abdelkareem MA, Sayed ET. Boosting the output power of PEM fuel cells by identifying best-operating conditions. Energy Convers Manag 2022;270.
[34] Chen X, Chen Y, Liu Q, Xu J, Liu Q, Li W, et al. Performance study on a stepped flow field design for bipolar plate in PEMFC. Energy Rep 2021;7:336–47.
[35] Mao X, Liu S, Tan J, Hu H, Lu C, Xuan D. Multi-objective optimization of gradient porosity of gas diffusion layer and operation parameters in PEMFC based on recombination optimization compromise strategy. Int J Hydrogen Energy 2023;48 (35):13294–307.
[36] Shen J, Tu Z, Chan SH. Enhancement of mass transfer in a proton exchange membrane fuel cell with blockage in the flow channel. Appl Therm Eng 2019;149: 1408–18.
[37] Yu Z, Xia L, Xu G, Wang C, Wang D. Improvement of the three-dimensional fine-mesh flow field of proton exchange membrane fuel cell (PEMFC) using CFD modeling, artificial neural network and genetic algorithm. Int J Hydrogen Energy 2022;47(82):35038–54.
[38] Huang Y-X, Cheng C-H, Wang X-D, Jang J-Y. Effects of porosity gradient in gas diffusion layers on performance of proton exchange membrane fuel cells. Energy 2010;35(12):4786–94.
[39] Meng H. A three-dimensional PEM fuel cell model with consistent treatment of water transport in MEA. J Power Sources 2006;162(1):426–35.
[40] Wang L. A parametric study of PEM fuel cell performances. Int J Hydrogen Energy 2003;28(11):1263–72.
[41] McKay MD, Beckman RJ, Conover WJ. A comparison of three methods for selecting values of input variables in the analysis of output from a computer code. Technometrics 2000;42(1):55–61.
[42] Li H-W, Xu B-S, Du C-H, Yang Y. Performance prediction and power density maximization of a proton exchange membrane fuel cell based on deep belief network. J Power Sources 2020;461.